



Improved mammalian retromer cryo-EM structures reveal a new assembly interface

Received for publication, March 4, 2022, and in revised form, August 30, 2022 Published, Papers in Press, September 26, 2022,
<https://doi.org/10.1016/j.jbc.2022.102523>

Amy K. Kendall^{1,2}, Mintu Chandra^{1,2}, Boyang Xie¹, William Wan^{2,3}, and Lauren P. Jackson^{1,2,3,*}

From the ¹Department of Biological Sciences, ²Center for Structural Biology, and ³Department of Biochemistry, Vanderbilt University, Nashville, Tennessee, USA

Edited by Phyllis Hanson

Retromer (VPS26/VPS35/VPS29 subunits) assembles with multiple sorting nexin proteins on membranes to mediate endosomal recycling of transmembrane protein cargoes. Retromer has been implicated in other cellular processes, including mitochondrial homeostasis, nutrient sensing, autophagy, and fission events. Mechanisms for mammalian retromer assembly remain undefined, and retromer engages multiple sorting nexin proteins to sort cargoes to different destinations. Published structures demonstrate mammalian retromer forms oligomers *in vitro*, but several structures were poorly resolved. We report here improved retromer oligomer structures using single-particle cryo-EM by combining data collected from tilted specimens with multiple advancements in data processing, including using a 3D starting model for enhanced automated particle picking in RELION. We used a retromer mutant (3KE retromer) that breaks VPS35-mediated interfaces to determine a structure of a new assembly interface formed by the VPS26A and VPS35 N-termini. The interface reveals how an N-terminal VPS26A arrestin saddle can link retromer chains by engaging a neighboring VPS35 N-terminus, on the opposite side from the well-characterized C-VPS26/N-VPS35 interaction observed within heterotrimers. The new interaction interface exhibits substantial buried surface area ($\sim 7000 \text{ \AA}^2$) and further suggests that metazoan retromer may serve as an adaptable scaffold.

Eukaryotic cells contain multiple membrane-enclosed organelles, which dynamically communicate with each other through membrane trafficking pathways. Trafficking ensures exchange of lipid and protein cargoes between donor and acceptor compartments, and trafficking events are spatiotemporally regulated by multiple large multiprotein complexes. Retromer (VPS26/VPS35/VPS29 subunits) is one important complex that plays a well-established role in protein sorting at endosomes by maintaining dynamic localization of hundreds of transmembrane proteins that traverse the endocytic system. Mammalian retromer associates with the cytosolic face of endosomes, where it functions to recycle receptors, transporters, and adhesion molecules. Retromer is thought to mediate retrograde recycling to the *trans*-Golgi

network (1–3) or to the plasma membrane (4–7) through sorting into tubular-vesicular carriers (reviewed in Refs. (8–10)). Retromer-dependent cargoes undergo selective trafficking to avoid sorting to late endosomes and subsequent degradation in lysosomes (11), which ensures cells maintain homeostasis of transmembrane cargoes at the plasma membrane and within the endolysosomal system. Retromer trafficking pathways become dysregulated in multiple ways, including aberrant protein processing (12) and sorting (13, 14). Disruptions to retromer trafficking in turn drive protein misfolding linked with neurological and neurodegenerative conditions, including Alzheimer's disease (15–17), Parkinson's disease (18), and Down's syndrome (19, 20). Retromer pathways can also be hijacked by both bacterial and viral pathogens (21, 22).

Retromer is now well established as an evolutionarily conserved heterotrimer that binds different sorting nexin (SNX) proteins to mediate cargo sorting from phosphatidylinositol-3-phosphate-enriched endosomal membranes. Retromer binds multiple SNX family members, including SNX-BARs, SNX3, and metazoan-specific SNX27 (reviewed recently in Refs. (10, 23, 24)). The retromer heterotrimer (formerly called cargo selective complex) has been implicated in direct cargo recognition in both mammalian cells (2, 3) and yeast (1, 25). More recently, SNX-BARs have been shown to bind cargo directly in mammalian cells (26, 27), and SNX3 promotes cargo recognition in both yeast (28, 29) and mammalian cells (30). Yeast SNX-BAR-retromer (31) and both yeast and mammalian SNX3-retromer (32) complexes have been shown to form tubules *in vitro*. SNXs may therefore be considered critical adaptors that promote membrane recruitment (5, 33), recognize cargo (6, 26, 30, 34, 35), and drive tubule formation (33).

From a structural viewpoint, multiple crystal (30, 36–38), single-particle cryo-EM (39), and cryo-electron tomography (cryo-ET) (31, 32) structures have revealed how retromer subunits fold in 3D space; how subunits interact to form a stable and elongated heterotrimer; and how heterotrimers assemble *in vitro* to form higher order oligomers in vitreous ice (39) or assembled on membranes with SNXs (31, 32). Briefly, VPS35 adopts an elongated α -helical solenoid fold. VPS26 exists as three orthologs in mammals (VPS26A/VPS26B/VPS26C) and adopts a bilobal arrestin-like fold

* For correspondence: Lauren P. Jackson, lauren.p.jackson@vanderbilt.edu.

Retromer cryo-EM reveals new interface

(38, 40). VPS26A and VPS26B bind the highly conserved VPS35 N terminus (38), whereas VPS26C binds VPS35-like (VPS35L) in the retriever complex (41). VPS29 contains a metallophosphoesterase fold (37, 42) that serves as a scaffold for binding the α -helical solenoid of the VPS35 C terminus (30, 36, 39). Cryo-ET reconstructions revealed how retromer assemblies with either SNX-BAR or SNX3 on membranes. Retromer assembles on top of either SNX-BAR dimers or SNX3 to form high V-shaped arches mediated by interactions between VPS35 subunits. Back-to-back VPS26 dimers mediate interactions with SNX-BARs or SNX3. In solution, mammalian retromer forms multiple oligomers, including the retromer heterotrimer; dimers of trimers; a tetramer of trimers; and extended flat chains (39). The existence of multiple oligomeric assemblies suggests that mammalian retromer may function as a flexible scaffold. Single-particle and biochemical data revealed critical residues in the VPS35–VPS35 assembly interface, which were tested biochemically and in yeast (39) and subsequently reported in cryo-ET reconstructions (32). The cryo-ET and single-particle reconstructions share several common themes. The mammalian VPS35–VPS35 dimer interface resembles yeast VPS35 dimers observed at the top of the V-shaped arches (31, 32). However, the curvature of the mammalian VPS35 interfaces observed in dimers and chains differs, which results in long and flat chains (39). In addition, mammalian retromer appears to form a VPS26A-mediated “tip-to-tip” dimer (39) that differs from back-to-back VPS26 dimers observed in the presence of SNX3 (32) or the yeast SNX-BAR, Vps5 (31). The mammalian VPS26 “chain link” interface was poorly resolved because particles exhibit severely preferred orientation. These data suggest that VPS26 may be capable of forming at least two different dimers, but the biological context of the “tip-to-tip” dimers remains unknown. Improved structural data for this putative interface are important so that structural models can be used to test function in cell culture or model organisms.

In this work, we report improved single-particle cryo-EM reconstructions of multiple mammalian retromer oligomers, including the heterotrimer, dimers of trimers, and two VPS35–VPS35 substructures. These improved structural models arise from multiple improvements implemented during data collection and processing. Acquisition of tilted datasets provided critical missing views for some particles. For some structures, early rounds of automated particle picking using a 3D starting model in RELION also provided additional views. Map sharpening followed by real-space refinement in PHENIX (43) resulted in improved heterotrimer reconstructions that allowed subunits to be assigned in maps more confidently. We further report a new structure of the N-VPS26A/N-VPS35 “chain link” interface using a retromer mutant (3KE mutant) that breaks VPS35 interfaces in chains (39). This new interface is formed by interactions between the VPS26A N-terminal arrestin fold with the N terminus of VPS35 in a neighboring heterotrimer. The presence of this particle *in vitro* suggests that retromer may be capable of forming a variety of assemblies, even in the absence of SNX proteins.

Results

Retromer heterotrimer

To generate improved reconstructions, we combined images from previously published data (39) with a new third dataset in which specimens were tilted to gain additional views (Fig. S1 and Table 1) (44). We obtained an improved heterotrimer reconstruction from 43,808 particles with an average resolution of 4.9 Å. Figure 1 formally compares this structure (panels A, C, E, and G; (44)) with the previously published version (panels B, D, F, and H; (39)). Critical missing views were acquired from the additional tilted dataset (Fig. 1E versus Fig. 1F). Map sharpening in PHENIX followed by several rounds of refinement and model building (see the Experimental procedures section) further improved the heterotrimer model (Fig. 1, A and G and Table 2). This structure demonstrates improved local resolution across the heterotrimer (Fig. 1, C and D). In the previous version (39), the N-VPS35/C-VPS26 interface was poorly resolved (Fig. 1, B and D) compared with the VPS35–VPS29 interface. In the new structure, the arrestin “saddle” fold of VPS26 is more clearly resolved (Fig. 1, A and G). Overall, improvements in both data collection and processing (see the Discussion section) played key roles in generating a higher quality reconstruction.

Retromer dimers of trimers

Retromer has been shown to form “dimers of heterotrimers” using both biophysical (39, 45) and structural (39) methods. In all reported conditions, formation of retromer dimers is mediated by the C-termini of VPS35 subunits. This dimer particle structure was very poorly resolved (average resolution of 18 Å) in previous studies (39). Others have reported improvements in single-particle structure determination by using a 3D starting model (46) in early rounds of automated particle picking. We employed this strategy in RELION using a previously obtained dataset (39) and a 3D starting model filtered to 20 Å to gain additional views of dimers in all possible orientations. We obtained an improved reconstruction (Figs. 2A and S2) from 70,214 particles with an average resolution of 7.0 Å. The presence of additional views substantially improved the structure (Fig. 2, E and F); overall resolution remains limited compared with the heterotrimer (Fig. 1).

Fitting rigid body models into Coulomb potential maps can be ambiguous, especially at modest resolution. Therefore, we systematically analyzed map handedness in the improved dimer reconstructions to generate the best model given the data. Briefly, we undertook the following approach (47). Both the original and flipped maps were used to perform a global search in which 3000 random orientations of the real-space refined heterotrimer model (details in the Experimental procedures section) were fitted as rigid bodies. A list of potential fits and crosscorrelation coefficients were generated for both maps (Fig. S3, A and D). Analyzing both maps with the top fitted model demonstrated the map with correct handedness (compare Fig. S3, B and C with Fig. S3, E and F).

Table 1
Summary of data collection and processing parameters

Parameter	3KE mutant particle and substructure	Dimer particle and VPS35–VPS35 substructure	Heterotrimer particle and VPS35–VPS35 substructure		
Microscope	Thermo Fisher FEI Titan Krios G3i Vanderbilt V-CEM	FEI Titan Krios Krios2 NRAMM	FEI Titan Krios Krios2 NRAMM	FEI Titan Krios Krios3 NRAMM	FEI Titan Krios Krios3 NRAMM
Cs	2.7 mm	2.7 mm	2.7 mm	2.7 mm	2.7 mm
Voltage	300 keV	300 keV	300 keV	300 keV	300 keV
Detector	ThermoFisher Falcon 3 direct electron detector	K2 Summit direct electron detector	K2 Summit direct electron detector	K2 Summit direct electron detector	K2 Summit direct electron detector
Magnification	120,000×	105,000×	105,000×	105,000×	105,000×
Pixel size	0.6811 Å/pix	1.096 Å/pix	1.096 Å/pix	1.06 Å/pix (rescaled to 1.096 Å/pix with motioncorr2 script)	1.06 Å/pix (rescaled to 1.096 Å/pix with motioncorr2 script)
Dose rate	1.4 e ⁻ /Å ² /s	~8 e ⁻ /Å ² /s	~8 e ⁻ /Å ² /s	~8 e ⁻ /Å ² /s	~8 e ⁻ /Å ² /s
Total dose	50 e ⁻ /Å ²	69.34 e ⁻ /Å ²	69.34 e ⁻ /Å ²	73.92 e ⁻ /Å ²	73.92 e ⁻ /Å ²
Tilt	±30°	N/A	N/A	N/A	±15°
Defocus range	-0.8 to -2.6 μm	-0.7 to 2.6 μm	-0.7 to 2.6 μm	-0.8 to -4.4 μm	-0.8 to -4.7 μm
Number of micrographs	4791	1480	1480	1299	891
Total particles (autopicked)	275,633	533,231	(250,500 particles selected from these datasets; (39))		207,026
Box size (Å)	436 × 436 Å (3KE) 215 × 215 Å (substructure)	351 × 351 Å (dimer) 180 × 180 Å (substructure)	241 × 241 Å (heterotrimer) 180 × 180 Å (substructure)	241 × 241 Å (heterotrimer) 180 × 180 Å (substructure)	241 × 241 Å (heterotrimer) 180 × 180 Å (substructure)
Particles in 2D classification	28,645 (3KE)	88,113 (dimer)	72,295 (heterotrimer)	72,295 (heterotrimer)	72,295 (heterotrimer)
Particles in final 3D model	19,184 (substructure) 26,641 (3KE)	70,214 (substructure) 70,214 (dimer)	69,381 (substructure) 43,808 (heterotrimer)	69,381 (substructure) 43,808 (heterotrimer)	69,381 (substructure) 43,808 (heterotrimer)
Symmetry	C1	C1	C1	C1	C1
Map resolution (masked FSC 0.143, RELION)	7.1 Å (3KE) 7.2 Å (substructure)	7.0 Å (dimer) 7.3 Å (substructure)	4.9 Å (heterotrimer) 4.5 Å (substructure)	4.9 Å (heterotrimer) 4.5 Å (substructure)	4.9 Å (heterotrimer) 4.5 Å (substructure)
B-factor (RELION)	-226.1 (3KE) -244.6 (substructure)	-227.0 (dimer) -150.1 (substructure)	-113.8 (heterotrimer) -226.3 (substructure)	-113.8 (heterotrimer) -226.3 (substructure)	-113.8 (heterotrimer) -226.3 (substructure)

VPS35/VPS35 substructures

Work from multiple laboratories has now demonstrated that both yeast and mammalian retromer form VPS35-mediated dimer interfaces in solution (39, 45) and when assembled on membranes (31, 32). We revisited two published substructures of VPS35/VPS35-mediated dimers (39) to generate improved reconstructions. The first substructure (Fig. 3A) was determined from VPS35-mediated dimers observed in elongated retromer chains (39). The second (Fig. 3B) was determined from retromer dimers after employing a 3D starting model in autopicking (previous section). The improved substructures revealed that both interfaces are asymmetrical (C1 symmetry; Fig. S1) and place specific electrostatic residues directly in the interface. These highly conserved residues (E615, D616, E617, K663, K701, and K705) were identified and tested in our previous work (39), and improved substructures presented here now provide the highest resolution views of this critical VPS35-mediated assembly interface (see the Discussion section).

A new oligomeric interface mediated by VPS26A and VPS35

One major limitation of our previous study was an inability to resolve a new dimer interface found in chain links and mediated by the N terminus of VPS26 subunits (chain interface II in Ref. (39)). These elongated chain particles exhibited extreme preferred orientation, so we used a

published mutant that breaks the VPS35/VPS35 dimer interface to generate a particle more tractable for cryo-EM studies. This retromer “3KE” mutant (39) enriches the heterogeneous retromer protein sample for particles that form dimers only at the VPS26 end. These smaller 3KE retromer mutant particles resemble the “f-hole” found on the body of a violin (Fig. 4). We obtained a tilted dataset from 3KE mutant retromer in the presence of a small cyclic peptide called RT-L4 (44), which has been shown to stabilize retromer structure. The presence of this peptide further enriched our protein sample for 3KE mutant particles. We generated a reconstruction of 3KE mutant dimers (Fig. 4A) from 26,641 particles using a 3D starting model (details in the Experimental procedures section) at an average resolution of 7.1 Å. One heterotrimer in this particle appears better resolved than the other (Fig. 4C), which may reflect how the particle behaves at the air–water interface. The RT-L4 peptide is extremely hydrophobic, and 3KE particles with RT-L4 tend to exhibit preferred orientation by aligning along the plane of the interface (Fig. 4D). We next determined a substructure centered on the chain link from 17,837 particles at an average resolution of 7.2 Å (Figs. S4 and S6), but this reconstruction provided no additional molecular information or improved resolution compared with the full particle. The chain link interface is mediated by a new interaction between the N-terminal arrestin saddle of VPS26 in one heterotrimer with the N terminus of VPS35 in a neighboring heterotrimer (Fig. 5A).

Retromer cryo-EM reveals new interface

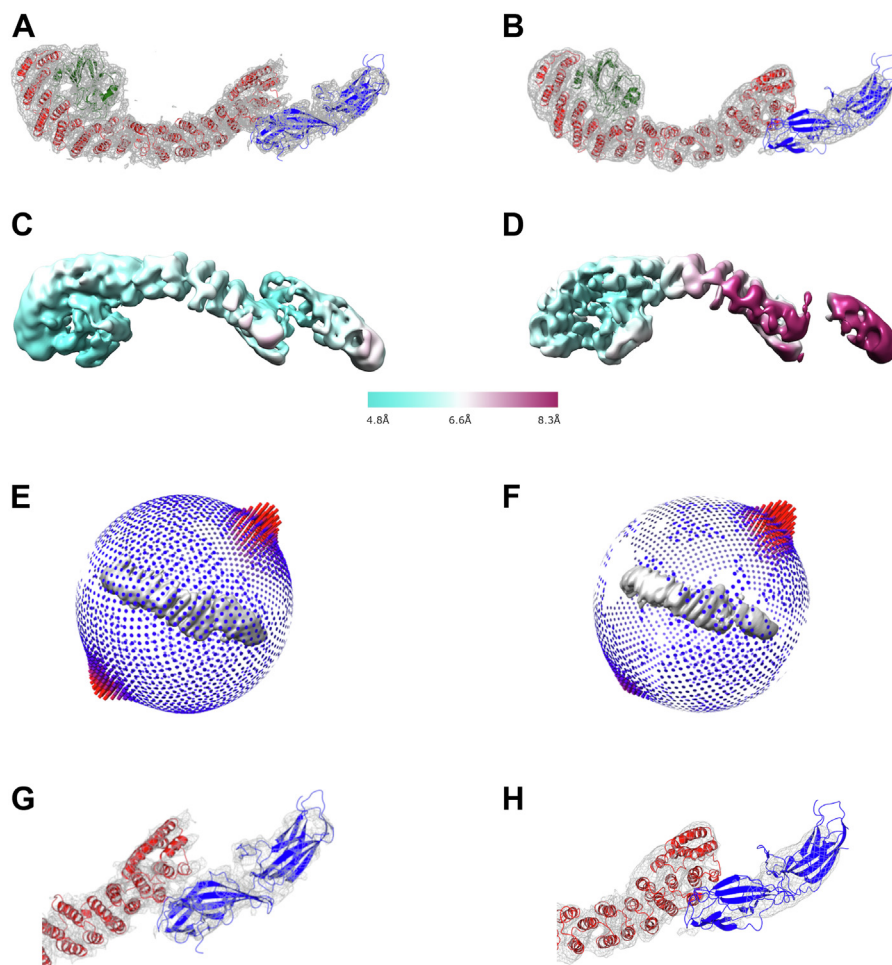


Figure 1. Single-particle reconstructions of the mammalian retromer heterotrimer. *A* and *B*, comparison of new 4.9 Å resolution (*A*) and previously reported (*B*) reconstructions of retromer heterotrimer with fitted models. VPS29 is shown as *green ribbons*, VPS35 as *red ribbons*, and VPS26 as *blue ribbons*. *C* and *D*, local resolution comparisons across new (*C*) and reported (*D*) heterotrimer reconstructions. *E* and *F*, angular distribution in new (*E*) and reported (*F*) reconstructions. *G* and *H*, close-up views of N-VPS35–C-VPS26 interface in new (*G*) and reported (*H*) reconstructions. All Coulomb potential maps were generated using CCP4MG and are shown at 5 σ contour level. Overall, acquisition of tilt data and improvements in data processing (details in text) resulted in an improved model.

Analysis of the N-VPS26/N-VPS35 interface

To further characterize the chain link interface, buried surface area was calculated using PISA (48) (Fig. 5). Within each retromer heterotrimer, interactions between N-VPS35 and C-VPS26 (Fig. 5A; *black and gray hatched circles*) bury

between 6387 and 6992 Å² (Fig. 5B). For comparison, the buried surface interface between N-VPS35 and C-VPS26 in the heterotrimer structure (Fig. 1) is 6178 Å². The slightly larger buried surface area values for the equivalent interface in 3KE mutant particles is consistent with RT-L4 playing a stabilizing

Table 2

MolProbity score summary of refined heterotrimer

All atom contacts	Clashscore (all atoms)	15.12	49th percentile ^a (N = 1784, all resolutions)
Protein geometry	Poor rotamers	31 (2.8%)	Goal: <0.3%
	Favored rotamers	1006 (91.3%)	Goal: >98%
	Ramachandran outliers	3 (0.25%)	Goal: <0.05%
	Ramachandran favored	1163 (96.2%)	Goal: >98%
	Ramachandran distribution (Z-score)	-2.35 ± 0.21	Goal: abs (Z score) <2
	MolProbity score ^b	2.28	60th percentile ^a (N = 27,675)
	C β deviations >0.25 Å	0 (0%)	Goal: 0
	Bad bonds	0/10,212 (0%)	Goal: 0%
	Bad angles	3/13,740 (0.02%)	Goal: <0.1%
Peptide omegas	<i>Cis</i> pralines	2/43 (4.7%)	Expected: <5%
Low-resolution criteria	CaBLAM outliers	15 (1.3%)	Goal: <1.0%
	Ca geometry outliers	3 (0.25%)	Goal: <0.5%
Additional validations	Chiral volume outliers	0/1542 (0%)	
	Waters with clashes	4/100 (4%)	

In the column results, the raw count is listed first with percentages in parentheses.

^a Hundredth percentile represents best among structures of comparable resolution; 0th percentile represents worst.

^b MolProbity score combines the clashscore, rotamer, and Ramachandran evaluations into a single score, normalized to be on same scale as X-ray resolution.

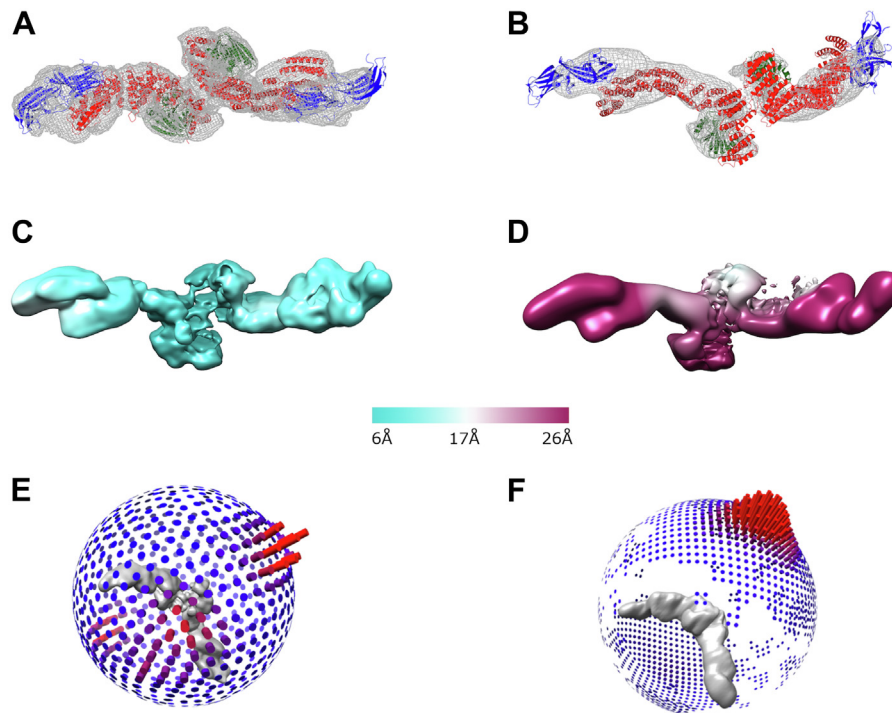


Figure 2. Single-particle reconstructions of retromer dimers of trimers. *A* and *B*, comparison of new (*A*) and previously reported (*B*) reconstructions of retromer dimers of heterotrimers with fitted models. Coulomb potential maps generated using CCP4MG are shown at 7σ (*A*) and 4σ (*B*) contour levels, respectively. *C* and *D*, local resolution comparisons across new (*C*) and reported (*D*) reconstructions. *E* and *F*, angular distribution in new (*E*) and reported (*F*) reconstructions.

role in this interface (44). The two new interfaces are located on the opposite face of N-VPS35, where each N-VPS35 interacts with an N-VPS26 subunit from a neighboring molecule (Fig. 5*A*; *black and gray circles*). Each new interface buries around 7000 \AA^2 (Fig. 5*B*). This analysis suggests that the new

interface buries approximately the same amount of surface as the well-characterized interaction between N-VPS35 and C-VPS26 within a retromer heterotrimer. The VPS35 N-terminal helix (residues 12–36) interacts specifically with two VPS26A β -strands (residues 48–56; 105–111) and their connecting

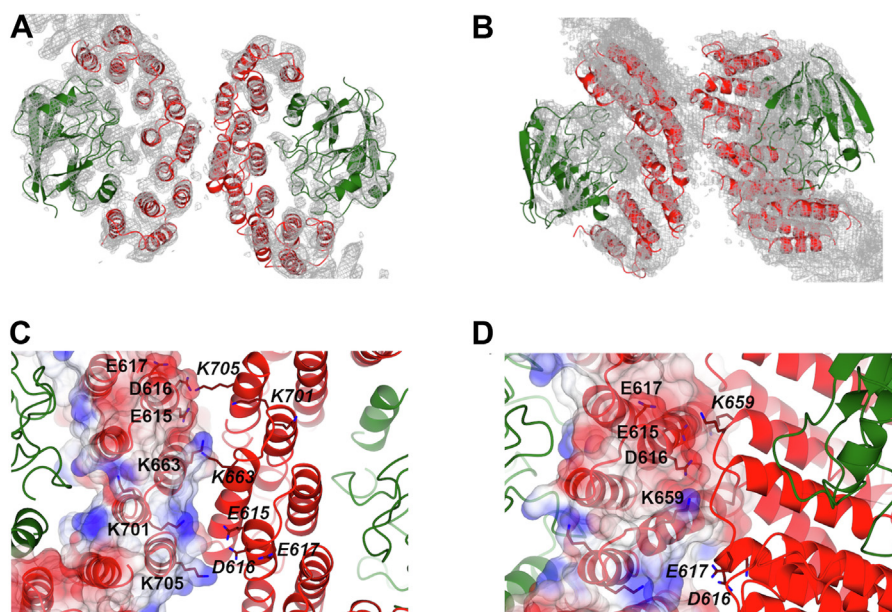


Figure 3. VPS35/VPS35 substructure reconstructions. *A*, VPS35/VPS35 substructure interface determined from retromer chains is shown with fitted model. *B*, VPS35/VPS35 substructure interface determined from retromer dimers of trimers (Fig. 2) is shown with fitted model. Coulomb potential maps generated using CCP4MG are shown at 4σ (*A* and *B*) contour levels. *C* and *D*, close-up views of VPS35/VPS35 dimer interfaces observed in flat chains (*C*) and dimers of trimers (*D*). Improvements in data processing resulted in reconstructions with higher resolution; these structures further support the presence of specific electrostatic residues (E615, D616, E617, K663, K701, and K705) mediating VPS35 dimer formation in asymmetric interfaces. Residues in the first dimer copy are labeled in *black text*, and residues in the second copy are labeled in *black italic text*.

Retromer cryo-EM reveals new interface

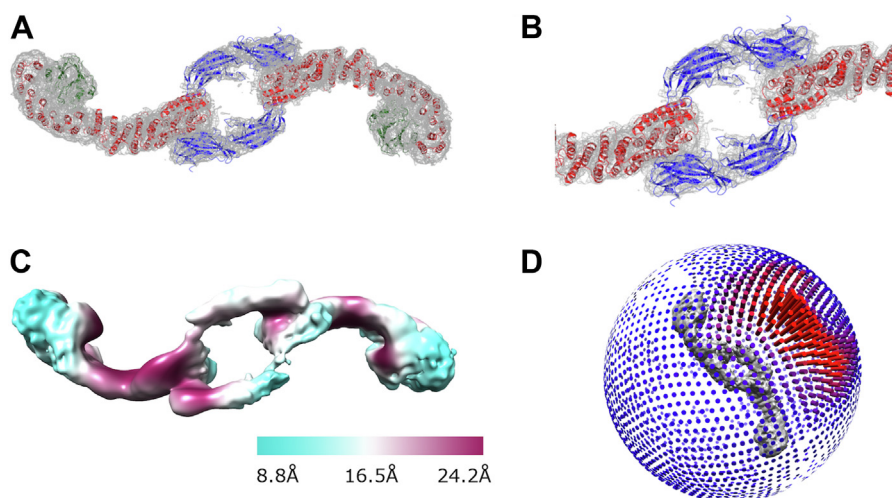


Figure 4. Single-particle reconstruction of the retromer 3KE mutant reveals a new interface. *A*, reconstruction of retromer 3KE particle. *B*, close-up view of the newly observed VPS26A/VPS35 interface, in which the N-terminal VPS26A arrestin saddle interacts with the N terminus of a neighboring VPS35 subunit. Coulomb potential maps generated using CCP4MG are shown at 7σ contour level. *C*, local resolution across 3KE mutant particle. *D*, angular distribution of 3KE mutant particle.

loops (residues 56–63; 101–105) (Fig. S7, *D* and *E*). Like the C-terminal VPS35/VPS35 interfaces (previous section), this N-VPS26/N-VPS35 interface does not exhibit twofold symmetry.

Discussion

Improved data acquisition and image processing

Two major improvements allowed us to generate better reconstructions of retromer oligomers and to determine the structure of a new interface. First, data acquisition from tilted specimens retrieved multiple and important missing views for several structures, including retromer dimer and 3KE mutant particles. We previously proposed that the VPS35 subunit could exhibit flexibility along the length of its α -helical sole-noid, as judged by local resolution along the heterotrimer particle (39). However, the new reconstruction (Fig. 1) instead suggests that the poor local resolution at the N terminus was instead driven by missing views. The decision to collect data from tilted specimens varies among practitioners, and our experience points to the importance of considering this as a data collection strategy. The second improvement arose from

using a 3D starting model in early rounds of automated particle picking for the retromer dimer and 3KE mutant particles. Use of a 3D starting model can help programs identify and include poorly sampled views, and this was particularly effective in generating improved structures of retromer dimer and 3KE mutant particles. However, we emphasize that this approach must be used with caution. Using the same 3D reference model for both template-based autopicking and 3D reconstruction has the potential to introduce substantial bias. Here, we have attempted to avoid introducing bias by using reference models from experimentally determined X-ray or cryo-ET structures for template-based autopicking. To further minimize reference model bias, we randomized the angles of picked particles to generate *ab initio* references prior to 3D classification and refinement for the dimer and 3KE particles.

C-VPS35 dimer interfaces

The VPS35/VPS35 interface (Fig. 3) we reported previously (39) includes several important conserved electrostatic residues observed at the top of retromer arches on membranes

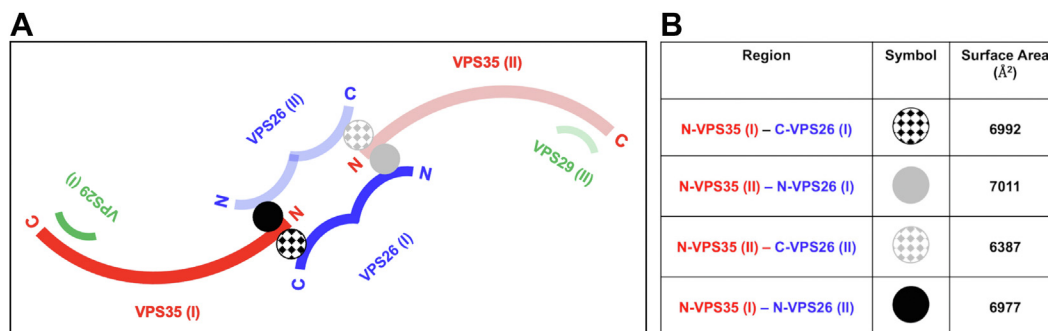


Figure 5. Analysis of retromer 3KE particle interfaces. *A*, schematic view of interactions observed in the retromer 3KE mutant particle. One heterotrimer is shown in dark colors (VPS29 in green, VPS35 in red, and VPS26 in blue), and the second heterotrimer is shown in transparent colors. Within each heterotrimer, N-VPS35 binds C-VPS26A (black and gray hatched circles). Each “chain link” structure is held together by an interaction between a VPS35 N terminus and the VPS26A N-terminal arrestin saddle in the neighboring heterotrimer (marked as black and gray circles). This interaction occurs on the opposite side from where the VPS35 N terminus interacts with a VPS26A subunit within its own heterotrimer. *B*, summary of buried surface area analysis between VPS35 and VPS26A (calculated using PISA, full details in text).

(31, 32). Both new substructures further support the placement of these residues in the interface. The improved structures also reveal that the interface is not twofold symmetrical, in agreement with reconstituted SNX3/retromer coats (32). We considered the possibility that VPS35-mediated dimers of heterotrimers observed in vitreous ice might represent V-shaped arches observed on membranes (31, 32). However, modeling arches into Coulomb potential maps after ascertaining correct handedness (Fig. S7A) does not support this. Extended assemblies such as retromer dimers may be affected during sample blotting, so it could be possible that arches observed on membranes have been flattened during the plunge freezing process by interactions at the air–water interface or by surface tension effects. Alternatively, dimers may represent a more loosely associated retromer structure that is further organized when it encounters relevant SNX proteins and cargoes on membranes.

N-VPS26/N-VPS35 interface

The interface between the N termini of VPS35 and VPS26A was previously observed in published structures of retromer chains (39) but is resolved more clearly in this work (Fig. 4) by using a retromer mutant that breaks the long chains into smaller particles. The interface buries a substantial amount of surface area (nearly 7000 Å²), suggesting it is a relatively stable particle *in vitro*. It is important to note this structure was determined in the presence of RT-L4 (44), a small molecule shown to stabilize the N-VPS35/C-VPS26 interface. The resolution of our structure is too low to locate or assign RT-L4, but in our hands, the presence of RT-L4 appeared to increase the number of 3KE retromer particles observed on grids. This suggests that stabilizing the retromer heterotrimer in turn stabilized its ability to form the N-VPS26A/N-VPS35 interface.

The resolution of both the 3KE particle structure and its substructure (~7 Å) is substantially lower than the C-VPS35 interface substructure determined from chains (~4.5 Å). The limited resolution makes it difficult to accurately identify specific residues mediating the interface with high confidence since side chains cannot be assigned. Alpha helices located in VPS35 interfaces (Fig. 3, A and B) can be more confidently fit, compared with the VPS26 β-sheets in the 7 Å resolution chain link substructure (Fig. S6). However, surface views of the interface suggest that the two N termini are complementary in overall shape (Fig. S7, D and E). We also note that the VPS26 N-terminal arrestin subdomain (Fig. S7F) is less conserved than the C-terminal subdomain (38), which may suggest that retromer from different species cannot build this interface.

The biological relevance of the N-VPS26A/N-VPS35 interface remains unknown. It will be important to test these structural models by mutating multiple residues along the interface to ascertain whether disruption drives cargo sorting or other defects. In addition to endosomal sorting, retromer has been implicated in other important cellular processes, including mitochondrial-derived vesicle formation (49) and regulation of mitochondrial membrane integrity (50), as well as nutrient sensing (51, 52) and autophagy (53). How retromer

regulates mitochondrial morphology is unknown (54). Recent work (55) indicates that a family of proteins called PROPPINs can compete with SNX proteins for retromer binding under certain conditions, and these PROPPIN–retromer interactions are linked to membrane fission events. Overall, the diversity of potential metazoan retromer functions suggests that retromer may also have expanded its structural repertoire to assemble in different ways. This is not unprecedented, as other trafficking proteins have been shown to assemble in different ways. One well-studied example is clathrin, since clathrin on its own forms different lattices (56), and clathrin-coated vesicles purified from brain exhibit a variety of geometries (57). It will be interesting to determine whether and how retromer may serve as a flexible scaffold to build different structures to mediate cellular events under a variety of conditions.

Experimental procedures

Reagents

Unless otherwise noted, all chemicals were purchased from Fisher.

Molecular biology and cloning

Both wildtype (37, 38) and 3KE mutant (39) retromer constructs have been published previously. Briefly, mouse VPS35 and VPS29 were placed in vector pGEX4T2 (GE Healthcare), whereas VPS26 was placed in in-house vector pMWkan. A two-stage quick-change mutagenesis protocol (58) was adapted to introduce three point mutations (K659E/K662E/K663E) into the VPS35 subunit to generate the retromer “3KE” electrostatic mutant that disrupts VPS35/VPS35 interface formation.

Protein expression and purification

Recombinant retromer protein (wildtype or 3KE mutant) was expressed and purified from *Escherichia coli* as previously described (39). Briefly, retromer plasmids were transformed into BL21(DE3) Rosetta2 pLysS cells (Millipore). Cells were grown to an absorbance at 600 nm between 0.8 and 1.0 and induced for 16 to 20 h at 22 °C with 0.4 mM IPTG. Cells were lysed by a disruptor (Constant Systems). The protein was purified in 10 mM Tris–HCl (pH 8.0), 200 mM NaCl, 2 mM β-mercaptoethanol using Glutathione Sepharose (GE Healthcare). Protein was cleaved overnight using thrombin (Recothrom; The Medicines Company) at room temperature and batch eluted in buffer. Retromer was further purified by gel filtration on a Superdex S200 16/60 analytical column (GE Healthcare) into 10 mM Tris–HCl (pH 8.0), 200 mM NaCl, or dialyzed into 20 mM Hepes (pH 8.2), 50 mM NaCl, and 2 mM DTT prior to vitrification.

Negative-stain grid preparation and screening

For screening negatively stained retromer samples, 10 μl of retromer at concentrations between 5 and 10 μg/ml were applied to continuous carbon film on 400 square mesh copper EM grids (Electron Microscopy Sciences) and washed twice with water. The grids were stained with 2% uranyl formate and

Retromer cryo-EM reveals new interface

1% uranyl acetate and air dried overnight. The grids were screened on a Thermo Fisher Morgagni microscope operating at 100 kV with an AMT 1 K × 1 K CCD camera (Center for Structural Biology Cryo-EM Facility, Vanderbilt University) to verify protein quality.

Cryo-EM sample preparation and data collection

Grid preparation

For cryo-EM, 2 μ l retromer at a concentration between 80 and 100 μ g/ml was applied to freshly glow discharged CF-2/2-2C C-Flat grids (Protochips) or Quantifoil R 1.2/1.3 300 mesh copper grids (Quantifoil Micro Tools GmbH). Grids were vitrified in liquid ethane using either a Thermo Fisher MarkIII or MarkIV Vitrobot, with blot times between 2 and 3.5 s and chamber conditions of 100% relative humidity and 8 to 20 °C.

Heterotrimer and flat substructure data collection

Micrographs from three separate data collections were used to generate the heterotrimer and flat substructure models. Each data collection is summarized later, and full details are also provided in Table 1. RELION-2 (59) and RELION-3 (60) were used for all image processing unless otherwise indicated.

Data collection 1—1480 micrographs were collected on a Thermo Fisher Titan Krios microscope at the National Resource for Automated Molecular Microscopy (NRAMM). The microscope operated at 300 keV and was equipped with a Gatan BioQuantum energy filter with a slit width of 20 eV, a spherical aberration (Cs) corrector, and a Gatan K2 Summit direct electron detector camera. The nominal magnification used during data collection was 105,000 \times , and the pixel size was 1.096 Å/pix. The total electron dose was 69.34e⁻/Å². Data collection was accomplished using Leginon (61). Images were motion corrected using MotionCor2 (62). The contrast transfer function (CTF) of each micrograph was determined using Gctf (63); defocus values for the data varied between -0.7 and -2.6 μ m.

Data collection 2—1299 micrographs were collected on a Thermo Fisher Titan Krios microscope at NRAMM. The microscope operated at 300 keV and was equipped with a Gatan BioQuantum energy filter with a slit width of 20 eV and a Gatan K2 Summit direct electron detector camera. The nominal magnification used during data collection was 105,000 \times , and the pixel size was 1.06 Å/pix. The total electron dose was 73.92e⁻/Å². Data collection was accomplished using Leginon. Images were motion corrected using MotionCor2, and micrographs from this data collection were rescaled to match the 1.096 Å/pix pixel size from the first data collection using an NRAMM script written for MotionCor2. The CTF of each micrograph was determined using Gctf; defocus values for the data varied between -0.8 and -4.4 μ m.

Data collection 3—891 micrographs were collected on a Thermo Fisher Titan Krios microscope at NRAMM. The microscope operated at 300 keV and was equipped with a Gatan BioQuantum energy filter with a slit width of 20 eV and a Gatan K2 Summit direct electron detector camera. The nominal magnification used during data collection was

105,000 \times , and the pixel size was 1.06 Å/pix. The total electron dose was 73.92e⁻/Å², and micrographs were collected at \pm 15° tilts. Data collection was accomplished using Leginon. Images were motion corrected using MotionCor2, and micrographs from this data collection were rescaled to match the 1.096 Å/pix pixel size from the first data collection using an NRAMM script written for MotionCor2. The CTF of each micrograph was determined using Gctf; defocus values for the data varied between -0.8 and -4.7 μ m.

Dimer and dimer substructure data collection

1480 micrographs were collected on a Thermo Fisher Titan Krios microscope at NRAMM. The microscope operated at 300 keV and was equipped with a Gatan BioQuantum energy filter with a slit width of 20 eV and a Gatan K2 Summit direct electron detector camera. The nominal magnification used during data collection was 105,000 \times , and the pixel size was 1.096 Å/pix. The total electron dose was 69.34e⁻/Å². Data collection was accomplished using Leginon. Images were motion corrected using MotionCor2. The CTF of each micrograph was determined using Gctf; defocus values for the data varied between -0.7 and -2.6 μ m. RELION-3 was used for all image processings unless otherwise indicated.

Retromer 3KE mutant and substructure data collection

4791 micrographs were collected on a Thermo Fisher Titan Krios G3i microscope in the Center for Structural Biology's Cryo-EM Facility at Vanderbilt. The microscope was operated at 300 keV and equipped with a Thermo Fisher Falcon3 direct electron detector camera. The nominal magnification used during data collection was 120,000 \times , and the pixel size was 0.6811 Å/pix. The total electron dose was 50e⁻/Å², and micrographs were collected at \pm 30° tilts. Data collection was accomplished using EPU (Thermo Fisher). Images were motion corrected using MotionCor2. The CTF of each micrograph was determined using Gctf; defocus values for the data varied between -0.8 and -2.6 μ m. RELION-3 was used for all image processings unless otherwise indicated.

Cryo-EM data processing

Heterotrimer

Data giving rise to our published retromer reconstruction (39) lacked tilted views; an additional dataset (data collection 3) was collected to add tilted views and to improve the reconstruction for this study. Several thousand particles were manually selected from dataset 3 to perform initial 2D classification and produce templates for autopicking. Template-based autopicking in RELION identified 207,026 particles, which were subjected to initial 2D and 3D classification and refinement as well as CTF refinement. About 250,500 particles from data collections 1 and 2 were imported to combine with data collection 3. Multiple rounds of 2D classification yielded 72,795 particles suitable to continue to 3D classification. Initial models for 3D classification (39) were filtered to 60 Å resolution for use in these experiments. The particles underwent multiple rounds of CTF refinement and Bayesian polishing to

produce a final set of 43,808 particles suitable for 3D refinement and postprocessing. The final masked heterotrimer model had a global resolution of 4.9 Å and a *B*-factor of −114 as determined in RELION.

VPS35/VPS35 sub-structure from retromer chains

Particles from the dataset containing all three data collections were windowed to a smaller box size that centered on the 35/35 interaction between two retromer molecules. Multiple rounds of 2D classification yielded 121,876 particles suitable to continue to 3D classification. Initial models for 3D classification (39) were filtered to 60 Å resolution for use in these experiments. The particles underwent multiple rounds of 3D classification to produce a final set of 69,381 particles suitable for 3D refinement and postprocessing. The final masked flat substructure model had a global resolution of 4.5 Å and a *B*-factor of −226 as determined in RELION.

Retromer dimers of trimers

Several thousand particles were manually selected to perform initial 2D and 3D classifications. Micrographs were then autopicked using a 20 Å low-pass filtered 3D model produced from initial rounds of manual picking; this template-based autopicking identified 533,231 particles. Multiple rounds of 2D classification yielded 509,447 particles suitable to continue to 3D classification. An *ab initio* model produced from the particle stack was filtered to 60 Å and used as an initial model for 3D classification. The particles underwent CTF refinement to produce a final set of 88,113 particles suitable for 3D refinement. The final masked dimer model had a global resolution of 7.0 Å and a *B*-factor of −227 as determined in RELION. We generated a z-flipped model of the dimer in Chimera (64). We then used the Chimera command “Fit in Map” to perform a global search testing 3000 random orientations of our real-space refined heterotrimer model filtered to 7 Å, with random displacement of 5 Å into each map. We generated a list of possible fits with crosscorrelations for both the z-flipped and unflipped maps of the dimer. Analyzing both maps with fitted rigid body models in Chimera demonstrated the map with correct handedness.

Dimer substructure

The particles contained in the refined set from the full dimer were windowed to a smaller box size that centered on the VPS35/VPS35 interaction between two retromer molecules. Multiple rounds of 2D classification yielded 70,214 particles suitable to continue to 3D classification. A windowed model of the refined full dimer structure was filtered to 60 Å and used as an initial model for 3D classification. A set of 17,840 particles continued to 3D refinement and postprocessing. The final masked dimer substructure model had a resolution of 7.3 Å and a *B*-factor of −150 as determined in RELION.

Retromer 3KE mutant

Micrographs were autopicked using a 20 Å low-pass filtered 3D model that had been produced in early rounds of

processing, and this template-based autopicking identified 275,633 particles. Multiple rounds of 2D classification yielded 28,645 particles suitable to continue to 3D classification. An *ab initio* model produced from the particle stack was filtered to 60 Å and used as an initial model for 3D classification. The particles underwent CTF refinement to produce a final set of 26,641 particles suitable for 3D refinement and postprocessing. The final masked model had a resolution of 7.1 Å and a *B*-factor of −226 as determined in RELION. To analyze map handedness, a z-flipped model of the retromer 3KE particle was generated in Chimera (64). We performed a global search testing 3000 random orientations of the real-space refined heterotrimer model (VPS26/VPS35/VPS29 as a single rigid body) filtered to 7 Å using the Chimera command “Fit in Map,” with random displacement of 5 Å into each map. This approach generated a list of potential fits with cross-correlations for both maps. Analyzing both maps with fitted rigid body models in Chimera demonstrated the map with correct handedness.

Retromer 3KE substructure

The particles contained in the refined set from the full f-hole were windowed to a smaller box size that centered on the 35/26 tails of the two retromer molecules. Multiple rounds of 2D classification yielded 19,184 particles suitable to continue to 3D classification. A windowed model of the refined full f-hole structure was filtered to 60 Å and used as an initial model for 3D classification. A set of 17,837 particles continued to 3D refinement, and the final masked f-hole substructure model had a resolution of 7.2 Å and a *B*-factor of −244 as determined in RELION.

Model building and docking

Models for VPS29 and the VPS35 C terminus were obtained from Protein Data Bank (PDB) code 2R17, whereas models for N-VPS35 and VPS26A were obtained from PDB code 5F0J. We omitted a flexible unstructured loop (amino acids 470–482) that is absent in all crystal structures. Rigid-body docking and map visualization were performed in Chimera using the command “Fit in Map.”

Retromer heterotrimer map sharpening

We used the 5 Å resolution Coulomb potential map to refine an atomic model of the retromer heterotrimer. The Coulomb potential map was further postprocessed in PHENIX by performing global or local *B*-factor sharpening using the program “Autosharpening” with a resolution cutoff at 5 Å. A PDB model containing all three retromer subunits (VPS26 and VPS35 from PDB code: 5F0J; VPS29 from PDB code: 2R17) was docked into the sharpened map and traced manually in Coot (65). Subsequently, several rounds of real-space refinement were performed in PHENIX (43). Overall statistics and geometry for the final model were analyzed using MolProbity (66, 67), and the quantitative metrics are summarized in Table 2. The overall RMSD between C_α atoms in the refined *versus* starting models was 1.1 Å. However, the overall

Retromer cryo-EM reveals new interface

geometric parameters of C α atoms are improved in the new model, suggesting the side chains may occupy more favorable conformations in the new model. While overall improvements in the model appear relatively small, the overall improvement in the sharpened map is substantial, showing that with current tools a cryo-EM map of modest quality at 5 Å resolution can be used to generate a fairly reliable model (Fig. 1).

Data visualization

All figures were generated using CCP4MG (68) or Chimera (64).

Data availability

Coulomb potential maps were deposited in the Electron Microscopy Data Bank (EMDB) with accession numbers EMD-24964, EMD-26342, and EMD-26341, corresponding to retromer heterotrimer, dimers, and 3KE mutant particles. Substructure maps were deposited for C-VPS35 dimers as EMD-26343 and EMD-26345 and for the 3KE mutant as EMD-26340. The heterotrimer dataset was first reported very briefly (44), but its refinement and analysis are reported here. Coordinates for this updated retromer heterotrimer were deposited in the PDB as 7U6F.

Supporting information—This article contains supporting information (69).

Acknowledgments—We thank Kevin Chen and Brett Collins for generously providing the RT-L4 peptide used in 3KE retromer sample preparation and data collection. Screening was conducted at the Center for Structural Biology Cryo-EM Facility at Vanderbilt University. Data collection was performed at the National Center for CryoEM Access and Training and the Simons Electron Microscopy Center located at the New York Structural Biology Center, supported by the National Institutes of Health Common Fund Transformative High Resolution Cryo-Electron Microscopy program (U24 GM129539) and by grants from the Simons Foundation (SF349247) and NY State Assembly.

Author contributions—L. P. J. conceptualization; A. K. K. and M. C. methodology; A. K. K. and M. C. formal analysis; A. K. K. and M. C. investigation; L. P. J. writing—original draft; W. W. and L. P. J. writing—review & editing; A. K. K. and M. C. visualization; W. W. and L. P. J. supervision; L. P. J. project administration; W. W. and L. P. J. funding acquisition.

Funding and additional information—A. K. K., M. C., B. X., and L. P. J. are supported by the National Institutes of Health grant (grant no.: R35GM119525). W. W. is supported by the National Institutes of Health grant (grant no.: DP2GM146321). The content is solely the responsibility of the authors and does not necessarily represent the official views of the National Institutes of Health.

Conflict of interest—The authors declare that they have no conflicts of interest with the contents of this article.

Abbreviations—The abbreviations used are: cryo-ET, cryo-electron tomography; CTF, contrast transfer function; NRAMM, National

Resource for Automated Molecular Microscopy; PDB, Protein Data Bank; SNX, sorting nexin.

References

1. Seaman, M. N., McCaffery, J. M., and Emr, S. D. (1998) A membrane coat complex essential for endosome-to-Golgi retrograde transport in yeast. *J. Cell Biol.* **142**, 665–681
2. Seaman, M. N. J. (2004) Cargo-selective endosomal sorting for retrieval to the Golgi requires retromer. *J. Cell Biol.* **165**, 111–122
3. Arighi, C. N., Hartnell, L. M., Aguilar, R. C., Haft, C. R., and Bonifacino, J. S. (2004) Role of the mammalian retromer in sorting of the cation-independent mannose 6-phosphate receptor. *J. Cell Biol.* **165**, 123–133
4. Lauffer, B. E. L., Melero, C., Temkin, P., Lei, C., Hong, W., Kortemme, T., et al. (2010) SNX27 mediates PDZ-directed sorting from endosomes to the plasma membrane. *J. Cell Biol.* **190**, 565–574
5. Temkin, P., Lauffer, B., Jäger, S., Cimermancic, P., Krogan, N. J., and von Zastrow, M. (2011) SNX27 mediates retromer tubule entry and endosome-to-plasma membrane trafficking of signalling receptors. *Nat. Cell Biol.* **13**, 715–721
6. Steinberg, F., Gallon, M., Winfield, M., Thomas, E. C., Bell, A. J., Heesom, K. J., et al. (2013) A global analysis of SNX27-retromer assembly and cargo specificity reveals a function in glucose and metal ion transport. *Nat. Cell Biol.* **15**, 461–471
7. Choy, R. W.-Y., Park, M., Temkin, P., Herring, B. E., Marley, A., Nicoll, R. A., et al. (2014) Retromer mediates a discrete route of local membrane delivery to dendrites. *Neuron* **82**, 55–62
8. Burd, C. G., and Cullen, P. J. (2014) Retromer: a master conductor of endosome sorting. *Cold Spring Harb. Perspect. Biol.* **6**, a016774
9. Simonetti, B., and Cullen, P. J. (2018) Endosomal sorting: architecture of the retromer coat. *Curr. Biol.* **28**, R1350–R1352
10. Chandra, M., Kendall, A. K., and Jackson, L. P. (2021) Toward understanding the molecular role of SNX27/retromer in human health and disease. *Front. Cell Dev. Biol.* **9**, 642378
11. Lu, L., and Hong, W. (2014) From endosomes to the trans-Golgi network. *Semin. Cell Dev. Biol.* **31**, 30–39
12. Fjorback, A., Seaman, M., Gustafsen, C., Mehmedbasic, A., Gokool, S., Wu, C., et al. (2012) Retromer binds the FANSHY sorting motif in SorLA to regulate amyloid precursor protein sorting and processing. *J. Neurosci.* **32**, 1467–1480
13. Andersen, O. M., Reiche, J., Schmidt, V., Gotthardt, M., Spoelgen, R., Behlke, J., et al. (2005) Neuronal sorting protein-related receptor sorLA/LR11 regulates processing of the amyloid precursor protein. *Proc. Natl. Acad. Sci. U. S. A.* **102**, 13461–13466
14. Yin, J., Liu, X., He, Q., Zhou, L., Yuan, Z., and Zhao, S. (2016) Vps35-dependent recycling of Trem2 regulates microglial function. *Traffic* **17**, 1286–1296
15. Reitz, C., Tokuhira, S., Clark, L. N., Conrad, C., Vonsattel, J.-P., Hazrati, L.-N., et al. (2011) SORCS1 alters amyloid precursor protein processing and variants may increase Alzheimer's disease risk. *Ann. Neurol.* **69**, 47–64
16. Mecozzi, V. J., Berman, D. E., Simoes, S., Vetanovetz, C., Awal, M. R., Patel, V. M., et al. (2014) Pharmacological chaperones stabilize retromer to limit APP processing. *Nat. Chem. Biol.* **10**, 443–449
17. Small, S. A., Kent, K., Pierce, A., Leung, C., Kang, M. S., Okada, H., et al. (2005) Model-guided microarray implicates the retromer complex in Alzheimer's disease. *Ann. Neurol.* **58**, 909–919
18. Zimprich, A., Benet-Pagès, A., Struhal, W., Graf, E., Eck, S. H., Offman, M. N., et al. (2011) A mutation in VPS35, encoding a subunit of the retromer complex, causes late-onset Parkinson disease. *Am. J. Hum. Genet.* **89**, 168–175
19. Curtis, M. E., Yu, D., and Praticò, D. (2020) Dysregulation of the retromer complex system in Down syndrome. *Ann. Neurol.* **88**, 137–147
20. Filippone, A., and Praticò, D. (2021) Endosome dysregulation in Down syndrome: a potential contributor to Alzheimer disease pathology. *Ann. Neurol.* **90**, 4–14
21. Romano-Moreno, M., Rojas, A. L., Williamson, C. D., Gershlick, D. C., Lucas, M., Isupov, M. N., et al. (2017) Molecular mechanism for the

- subversion of the retromer coat by the Legionella effector RidL. *Proc. Natl. Acad. Sci. U. S. A.* **114**, E11151–E11160
22. Daniloski, Z., Jordan, T. X., Wessels, H.-H., Hoagland, D. A., Kasela, S., Legut, M., *et al.* (2021) Identification of required host factors for SARS-CoV-2 infection in human cells. *Cell* **184**, 92–105.e16
 23. Sztul, E., Chen, P.-W., Casanova, J. E., Cherfils, J., Dacks, J. B., Lambright, D. G., *et al.* (2019) ARF GTPases and their GEFs and GAPs: concepts and challenges. *Mol. Biol. Cell* **30**, 1249–1271
 24. Chandra, M., Kendall, A. K., and Jackson, L. P. (2020) Unveiling the cryo-EM structure of retromer. *Biochem. Soc. Trans.* **48**, 2261–2272
 25. Nothwehr, S. F., Ha, S. A., and Bruinsma, P. (2000) Sorting of yeast membrane proteins into an endosome-to-Golgi pathway involves direct interaction of their cytosolic domains with Vps35p. *J. Cell Biol.* **151**, 297–309
 26. Kvainickas, A., Jimenez-Orgaz, A., Nägele, H., Hu, Z., Dengjel, J., and Steinberg, F. (2017) Cargo-selective SNX-BAR proteins mediate retromer trimer independent retrograde transport. *J. Cell Biol.* **216**, 3677–3693
 27. Simonetti, B., Paul, B., Chaudhari, K., Weeratunga, S., Steinberg, F., Gorla, M., *et al.* (2019) Molecular identification of a BAR domain-containing coat complex for endosomal recycling of transmembrane proteins. *Nat. Cell Biol.* **21**, 1219–1233
 28. Harrison, M. S., Hung, C.-S., Liu, T., Christiano, R., Walther, T. C., and Burd, C. G. (2014) A mechanism for retromer endosomal coat complex assembly with cargo. *Proc. Natl. Acad. Sci. U. S. A.* **111**, 267–272
 29. Bean, B. D. M., Davey, M., and Conibear, E. (2017) Cargo selectivity of yeast sorting nexins. *Traffic* **18**, 110–122
 30. Lucas, M., Gershlick, D. C., Vidaurrezaga, A., Rojas, A. L., Bonifacino, J. S., and Hierro, A. (2016) Structural mechanism for cargo recognition by the retromer complex. *Cell* **167**, 1623–1635.e14
 31. Kovtun, O., Leneva, N., Bykov, Y. S., Ariotti, N., Teasdale, R. D., Schaffer, M., *et al.* (2018) Structure of the membrane-assembled retromer coat determined by cryo-electron tomography. *Nature* **561**, 561–564
 32. Leneva, N., Kovtun, O., Morado, D. R., Briggs, J. A. G., and Owen, D. J. (2021) Architecture and mechanism of metazoan retromer:SNX3 tubular coat assembly. *Sci. Adv.* **7**, eabf8598
 33. Carlton, J., Bujny, M., Peter, B. J., Oorschot, V. M. J., Rutherford, A., Mellor, H., *et al.* (2004) Sorting nexin-1 mediates tubular endosome-to-TGN transport through coincidence sensing of high-curvature membranes and 3-phosphoinositides. *Curr. Biol.* **14**, 1791–1800
 34. Simonetti, B., Danson, C. M., Heesom, K. J., and Cullen, P. J. (2017) Sequence-dependent cargo recognition by SNX-BARs mediates retromer-independent transport of CI-MPR. *J. Cell Biol.* **216**, 3695–3712
 35. Stochlic, T. I., Setty, T. G., Sitaram, A., and Burd, C. G. (2007) Grd19/Snx3p functions as a cargo-specific adapter for retromer-dependent endocytic recycling. *J. Cell Biol.* **177**, 115–125
 36. Hierro, A., Rojas, A. L., Rojas, R., Murthy, N., Effantin, G., Kajava, A. V., *et al.* (2007) Functional architecture of the retromer cargo-recognition complex. *Nature* **449**, 1063–1067
 37. Collins, B. M., Skinner, C. F., Watson, P. J., Seaman, M. N., and Owen, D. J. (2005) Vps29 has a phosphoesterase fold that acts as a protein interaction scaffold for retromer assembly. *Nat. Struct. Mol. Biol.* **12**, 594–602
 38. Collins, B. M., Norwood, S. J., Kerr, M. C., Mahony, D., Seaman, M. N. J., Teasdale, R. D., *et al.* (2008) Structure of Vps26B and mapping of its interaction with the retromer protein complex. *Traffic* **9**, 366–379
 39. Kendall, A. K., Xie, B., Xu, P., Wang, J., Burcham, R., Frazier, M. N., *et al.* (2020) Mammalian retromer is an adaptable scaffold for cargo sorting from endosomes. *Structure* **28**, 393–405.e4
 40. Shi, H., Rojas, R., Bonifacino, J. S., and Hurley, J. H. (2006) The retromer subunit Vps26 has an arrestin fold and binds Vps35 through its C-terminal domain. *Nat. Struct. Mol. Biol.* **13**, 540–548
 41. McNally, K. E., Faulkner, R., Steinberg, F., Gallon, M., Ghai, R., Pim, D., *et al.* (2017) Retriever is a multiprotein complex for retromer-independent endosomal cargo recycling. *Nat. Cell Biol.* **19**, 1214–1225
 42. Wang, D., Guo, M., Liang, Z., Fan, J., Zhu, Z., Zang, J., *et al.* (2005) Crystal structure of human vacuolar protein sorting protein 29 reveals a phosphodiesterase/nuclease-like fold and two protein-protein interaction sites. *J. Biol. Chem.* **280**, 22962–22967
 43. Adams, P. D., Afonine, P. V., Bunkóczi, G., Chen, V. B., Davis, I. W., Echols, N., *et al.* (2010) PHENIX: a comprehensive, Python-based system for macromolecular structure solution. *Acta Crystallogr. D Biol. Crystallogr.* **66**, 213–221
 44. Chen, K.-E., Guo, Q., Hill, T. A., Cui, Y., Kendall, A. K., Yang, Z., *et al.* (2021) De novo macrocyclic peptides for inhibiting, stabilizing, and probing the function of the retromer endosomal trafficking complex. *Sci. Adv.* **7**, eabg4007
 45. Norwood, S. J., Shaw, D. J., Cowieson, N. P., Owen, D. J., Teasdale, R. D., and Collins, B. M. (2010) Assembly and solution structure of the core retromer protein complex. *Traffic* **12**, 56–71
 46. Greber, B. J., Remis, J., Ali, S., and Nogales, E. (2021) 2.5 Å-resolution structure of human CDK-activating kinase bound to the clinical inhibitor ICEC0942. *Biophys. J.* **120**, 677–686
 47. Wan, W., Kolesnikova, L., Clarke, M., Koehler, A., Noda, T., Becker, S., *et al.* (2017) Structure and assembly of the Ebola virus nucleocapsid. *Nature* **551**, 394–397
 48. Krissinel, E., and Henrick, K. (2007) Inference of macromolecular assemblies from crystalline state. *J. Mol. Biol.* **372**, 774–797
 49. Braschi, E., Goyon, V., Zunino, R., Mohanty, A., Xu, L., and McBride, H. M. (2010) Vps35 mediates vesicle transport between the mitochondria and peroxisomes. *Curr. Biol.* **20**, 1310–1315
 50. Farmer, T., O'Neill, K. L., Naslavsky, N., Luo, X., and Caplan, S. (2019) Retromer facilitates the localization of Bcl-xL to the mitochondrial outer membrane. *Mol. Biol. Cell* **30**, 1138–1146
 51. Kvainickas, A., Nägele, H., Qi, W., Dokládal, L., Jimenez-Orgaz, A., Stehl, L., *et al.* (2019) Retromer and TBC1D5 maintain late endosomal RAB7 domains to enable amino acid-induced mTORC1 signaling. *J. Cell Biol.* **218**, 3019–3038
 52. Hesketh, G. G., Papazotos, F., Pawling, J., Rajendran, D., Knight, J. D. R., Martinez, S., *et al.* (2020) The GATOR-Rag GTPase pathway inhibits mTORC1 activation by lysosome-derived amino acids. *Science* **370**, 351–356
 53. Roy, S., Leidal, A. M., Ye, J., Ronen, S. M., and Debnath, J. (2017) Autophagy-dependent shuttling of TBC1D5 controls plasma membrane translocation of GLUT1 and glucose uptake. *Mol. Cell* **67**, 84–95.e5
 54. Farmer, T., Naslavsky, N., and Caplan, S. (2018) Tying trafficking to fusion and fission at the mighty mitochondria. *Traffic* **19**, 569–577
 55. Courtellement, T., De Leo, M. G., Gopaladass, N., and Mayer, A. (2022) CROP: a retromer-PROPPIN complex mediating membrane fission in the endo-lysosomal system. *EMBO J* **41**, e109646
 56. Morris, K. L., Jones, J. R., Halebian, M., Wu, S., Baker, M., Armache, J.-P., *et al.* (2019) Cryo-EM of multiple cage architectures reveals a universal mode of clathrin self-assembly. *Nat. Struct. Mol. Biol.* **26**, 890–898
 57. Paraan, M., Mendez, J., Sharum, S., Kurtin, D., He, H., and Stagg, S. M. (2020) The structures of natively assembled clathrin-coated vesicles. *Sci. Adv.* **6**, eaba8397
 58. Wang, W., and Malcolm, B. A. (1999) Two-stage PCR protocol allowing introduction of multiple mutations, deletions and insertions using QuikChange site-directed mutagenesis. *Biotechniques* **26**, 680–682
 59. Scheres, S. H. W. (2012) Relion: implementation of a bayesian approach to cryo-EM structure determination. *J. Struct. Biol.* **180**, 519–530
 60. Zivanov, J., Nakane, T., Forsberg, B. O., Kimanius, D., Hagen, W. J., Lindahl, E., *et al.* (2018) New tools for automated high-resolution cryo-EM structure determination in RELION-3. *Elife* **7**, e42166
 61. Carragher, B., Kisseberth, N., Kriegman, D., Milligan, R. A., Potter, C. S., Pulokas, J., *et al.* (2000) Leginon: an automated system for acquisition of images from vitreous ice specimens. *J. Struct. Biol.* **132**, 33–45
 62. Zheng, S. Q., Palovcak, E., Armache, J.-P., Verba, K. A., Cheng, Y., and Agard, D. A. (2017) MotionCorr2: anisotropic correction of beam-induced motion for improved cryo-electron microscopy. *Nat. Methods* **14**, 331–332
 63. Zhang, K. (2016) Gctf: real-time CTF determination and correction. *J. Struct. Biol.* **193**, 1–12

Retromer cryo-EM reveals new interface

64. Pettersen, E. F., Goddard, T. D., Huang, C. C., Couch, G. S., Greenblatt, D. M., Meng, E. C., *et al.* (2004) UCSF Chimera—a visualization system for exploratory research and analysis. *J. Comp. Chem.* **25**, 1605–1612
65. Emsley, P., and Cowtan, K. (2004) Coot: model-building tools for molecular graphics. *Acta Crystallogr. D Biol. Crystallogr.* **60**(Pt 12 Pt 1), 2126–2132
66. Chen, V. B., Arendall, W. B., Headd, J. J., Keedy, D. A., Immormino, R. M., Kapral, G. J., *et al.* (2010) MolProbity: all-atom structure validation for macromolecular crystallography. *Acta Crystallogr. D Biol. Crystallogr.* **66**, 12–21
67. Williams, C. J., Headd, J. J., Moriarty, N. W., Prisant, M. G., Videau, L. L., Deis, L. N., *et al.* (2018) MolProbity: more and better reference data for improved all-atom structure validation. *Protein Sci.* **27**, 293–315
68. McNicholas, S., Potterton, E., Wilson, K. S., and Noble, M. E. M. (2011) Presenting your structures: the CCP4mg molecular-graphics software. *Acta Crystallogr. D Biol. Crystallogr.* **67**, 386–394
69. Ashkenazy, H., Abadi, S., Martz, E., Chay, O., Mayrose, I., Pupko, T., *et al.* (2016) ConSurf 2016: an improved methodology to estimate and visualize evolutionary conservation in macromolecules. *Nucl Acids Res.* <https://doi.org/10.1093/nar/gkw408>